Hindawi
Shock and Vibration
Volume 2020, Article ID 8138726, 11 pages
https://doi.org/10.1155/2020/8138726

Research Article

Influence of Hysteresis on the Vibration Control of a Smart Beam with a Piezoelectric Actuator by the Bouc–Wen Model

Ting Zhang

School of Mechanical and Automotive Engineering, Shanghai University of Engineering Science, Shanghai 201620, China

Correspondence should be addressed to Ting Zhang; ztwcl@sjtu.edu.cn

Received 10 October 2019; Revised 30 January 2020; Accepted 8 February 2020; Published 9 March 2020

Academic Editor: Kumar V. Singh

The hysteresis property in a smart structure has attracted much attention from researchers for several decades. Hysteresis not only affects the response precision of the smart structure but also threatens the stability of the system. This paper focuses on how the hysteresis property influences the control effect of vibration suppression for a smart beam. Furthermore, the Bouc–Wen model is adopted to describe the hysteresis property of a smart beam and the hysteresis parameters of the hysteresis model are identified with a genetic algorithm. Based on the identification results, the hysteresis model is validated to represent the hysteresis property of the smart beam. Based on the hysteresis model, model reference adaptive control is designed to explore the influence of hysteresis on the vibration control of the smart beam. With some simulations and experiments, it is found that the vibration control effect is influenced when the hysteresis item changes. The vibration control effect will be improved when the hysteresis coefficient in the Bouc–Wen model, as the expected objective model of the adaptive reference model, is within a proper numerical range where the control system is stable. Furthermore, when the time delay is considered in the closed-loop control system, the principle of the hysteresis influence is different. The results indicate that the hysteresis property affects not only the control effect but also the stability of the control system for a smart cantilever beam.

1. Introduction

Hysteresis is a common nonlinearity of piezoelectric materials [1–3]. Hysteresis is a lagging phenomenon where a physical effect on the smart material lags behind its cause. When a smart material acts as an actuator or a sensor of space structure, the response of the smart structure lags behind the input excitation of the system [4, 5]. The nonlinearity not only affects the control precision of the smart structure with a control law but also threatens the stability of the control system [6]. Therefore, it is an urgent challenge to address how the hysteresis property exactly influences the control precision and the stability of the control system.

Some researchers have not considered the hysteresis property in their studies when performing active control investigations of smart structures [7]. Furthermore, some linear control laws are commonly designed based on a linear model for the smart structure. For example, PID control was implemented to damp both the free and forced vibrations of a thin-walled structure and compared with LQR optimal control [8], a new intelligent methodology was introduced to mitigate the vibration response of flexible cantilever plates [9], and a minimax-linear quadratic Gaussian controller was designed based on an uncertain system model for the positioning of a piezoelectric tube scanner used in an atomic force microscope [10]. These linear control approaches are limited in terms of their applications to linear system models. Once the controlled system is requested to have high precision and a fast response, these linear control methods cannot meet the requirements. Therefore, modeling the hysteresis nonlinearities of smart structures is important for designing a controller to explore the influence of hysteresis on the control of the smart structures.

At present, the hysteresis modeling approaches include Preisach model [11], Prandtl–Ishlinskii (PI) model [12–14], and Bouc–Wen model [15]. The Preisach model and Prandtl–Ishlinskii model are rate-independent hysteresis models and are also phenomenological hysteresis models

[16]. Based on the two types of models, the main control laws were adopted with only their inverse hysteresis model as open-loop control to compensate for the hysteresis property of the smart structure [17, 18]. It is difficult to design closed-loop control strategies on account of the two models. However, the Bouc–Wen model is a rate-dependent model and a physics-based hysteresis model. The hysteresis parameters of the Bouc–Wen model are easily identified [19–21]. In addition, feedback or feedforward control may be easily realized with its inverse model and a certain control law. The control laws applied to suppress vibration mainly include PID control [22], adaptive control [6, 23], robust control [24], and intelligent control [25, 26]. These control laws have been used to compensate for the hysteresis property or track the expected trajectory. However, few studies have analyzed how to affect the control result by the hysteresis of a smart structure. Furthermore, compared with other control methods, the adaptive control has strongly robust, adaptive, and anti-interference properties. Because of these advantages, the model reference adaptive control [23, 27] is adopted to explore the influence of hysteresis on the control effect of vibration suppression of smart structures with the Bouc–Wen model in this paper.

The rest of this paper is organized as follows. A dynamic model for a smart flexible beam, dynamic model validations, and stability analyses are presented in Section 2. Model reference adaptive control with the Bouc–Wen model as an expected reference model is introduced in Section 3. Simulations and experiments on vibration suppression of the smart beam are discussed in Section 4. Finally, conclusions are presented in Section 5.

2. Dynamic Modeling of a Smart Cantilever Beam

2.1. A Model of a Smart Beam with the Bouc–Wen Equation. A flexible beam bonded with a piezoelectric actuator is shown in Figure 1. The smart beam is regarded as an Euler–Bernoulli beam, and its bending vibration is assumed to be $\omega(x,t)$. Thus, the dynamic partial differential equation of the flexible beam is given as

$$m(x)\frac{\partial^2\omega(x,t)}{\partial t^2}+c(x)\frac{\partial\omega(x,t)}{\partial t}+\frac{\partial^2}{\partial x^2}\left[\mathrm{EI}(x)\frac{\partial^2\omega(x,t)}{\partial x^2}\right] = Q(x,t), \tag{1}$$

where m is the linear mass, c is the damping coefficient, E is the elasticity modulus, I is the inertia moment, and Q is a line distributed force.

The constitutive equation of the piezoelectric material is described as

$$\begin{cases} s_1 = s_{11}^E S_1 + d_{31}E_3, \\ D_3 = d_{31}S_1 + \varepsilon_{33}^X E_3, \end{cases} \tag{2}$$

where s_1 and S_1 are the strain and stress, respectively, E_3 is the electric field, and D_3 is the electric displacement. Moreover, s_{11}^E, d_{31}, and ε_{33}^X are the elastic compliance, piezoelectric strain, and dielectric constants, respectively.

When there is no external stress and the electric field is $E_3 = U/t_p$ (U is the external applied voltage and t_p is the thickness of the piezoelectric actuator), the strain of the piezoelectric actuator is derived as

$$s = \frac{d_{31}}{t_p}U(x,t). \tag{3}$$

The stress is obtained as

$$S = E_p s, \tag{4}$$

where E_p is the elasticity modulus of the piezoelectric actuator.

Therefore, the moment M of force is expressed as

$$M(x,t) = \int_A S y dA_p, \tag{5}$$

where A_p is the cross-sectional area of the piezoelectric actuator.

Substituting equations (3) and (4) into equation (5), the moment is obtained to be as follows:

$$\begin{aligned} M(x,t) &= \left(\int_{(t_b/2)}^{(t_b/2)+t_p} E_p\frac{d_{31}}{t_p}y h_p \mathrm{d}y\right)U(x,t) \\ &= K_p U(x,t), \end{aligned} \tag{6}$$

where t_b and h_p are the thickness of the beam and the height of the piezoelectric actuator, respectively, and $K_p = (1/2)h_p d_{31}E_p(t_b + t_p)$.

Furthermore, the input voltage U is expressed as

$$U(x,t) = V(t)H(x), \tag{7}$$

where $V(t)$ is a time function and $H(x)$ is the Heaviside function.

The moment of force and line distributed force are related as follows:

$$Q(x,t) = \frac{d^2M}{dx^2}. \tag{8}$$

Substituting equations (6) and (8) into equation (1) yields

$$\begin{aligned} &m(x)\frac{\partial^2\omega(x,t)}{\partial t^2}+c(x)\frac{\partial\omega(x,t)}{\partial t}+\frac{\partial^2}{\partial x^2}\left[\mathrm{EI}(x)\frac{\partial^2\omega(x,t)}{\partial x^2}\right] \\ &= \frac{\partial^2}{\partial x^2}\left[K_p V(t)\left[H(x-x_1)-H(x-x_0)\right]\right]. \end{aligned} \tag{9}$$

The bending vibration $\omega(x,t)$ is obtained by a superposition of vibration modes as

$$\omega(x,t) = \sum_{i=1}^{\infty}\phi_i(x)q_i(t), \tag{10}$$

where $\phi_i(x)$ is a mode and $q_i(t)$ is the generalized coordinate:

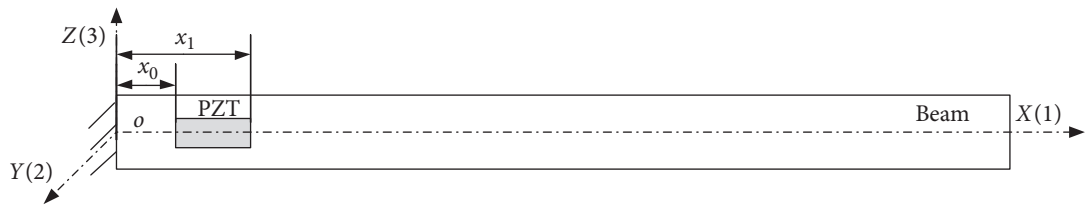

Figure 1: Smart beam.

$$\phi_i(x) = \cosh(\beta_i x) - \cos(\beta_i x) - \frac{\sinh(\beta_i l_b) - \sin(\beta_i l_b)}{\cosh(\beta_i l_b) + \cos(\beta_i l_b)} \cdot [\sinh(\beta_i x) - \sin(\beta_i x)]. \tag{11}$$

where $\beta_1 l_b = 1.875$, $\beta_2 l_b = 4.694$, $\beta_3 l_b = 7.855$,. . ., and l_b is the length of the beam.

Substituting equation (10) into equation (9) yields

$$\sum_{i=1}^{\infty} m(x)\phi_i(x)\ddot{q}_i(t) + \sum_{i=1}^{\infty} c(x)\phi_i(x)\dot{q}_i(t) + \sum_{i=1}^{\infty} \frac{d^2}{dx^2}\left[\mathrm{EI}(x)\frac{d^2\phi_i(x)}{dx^2}\right] q_i(t) = \frac{\partial^2}{\partial x^2}\left\{K_p V(t)\left[H(x-x_1) - H(x-x_0)\right]\right\}. \tag{12}$$

Because of the mode shape orthogonality,

$$\int \phi_i(x)\phi_j(x)\mathrm{d}x = 0, \quad i \neq j. \tag{13}$$

It is assumed that $EI(x)(d^4\phi_i(x)/dx^4) = m\Omega_i^2\phi_i(x)$. The mode $\phi_j(x)$ is multiplied by both sides of equation (12) ; then, equation (12) is integrated with respect to x as follows:

$$\left[\int_0^{l_b} \phi_j(x)m(x)\phi_j(x)\mathrm{d}x\right]\ddot{q}_j(t) + \left[\int_0^{l_b} \phi_j(x)c(x)\phi_j(x)\mathrm{d}x\right]\dot{q}_j(t) + \left[\int_0^{l_b} \phi_j(x)\mathrm{EI}(x)\beta_j^4\phi_j(x)\mathrm{d}x\right]q_j(t) = K_p V(t)\left[\phi_j'(x_1) - \phi_j'(x_0)\right]. \tag{14}$$

The natural frequency is obtained as

$$\Omega_j = \beta_j^2\sqrt{\frac{\int_0^{l_b} E_b I_b \phi_j^2(x)\mathrm{d}x + \int_{x_0}^{x_1} E_p I_p \phi_j^2(x)\mathrm{d}x}{\int_0^{l_b} m_b\phi_j^2(x)\mathrm{d}x + \int_{x_0}^{x_1} m_b\phi_j^2(x)\mathrm{d}x}}, \tag{15}$$

where $m_b$and m_p are the masses of the cantilever beam and the piezoelectric patch, respectively, I_b and I_p are the moments of inertia of the cantilever beam, and E_p is the elastic modulus of the cantilever beam.

Then, assuming $M_j = \int_0^{l_b} \phi_j(x)m\phi_j(x)\mathrm{d}x$ and $C_j = \int_0^{l_b} \phi_j(x)c\phi_j(x)\mathrm{d}x$, equation (15) is expressed as

$$M_j\ddot{q}_j(t) + C_j\dot{q}_j(t) + M_j\Omega_j^2 q_j(t) = K_p V(t)\left[\phi_j'(x_1) - \phi_j'(x_0)\right]. \tag{16}$$

Both sides of equation (17) are multiplied by $(1/M_j)$, yielding

$$\ddot{q}_j(t) + 2\zeta_j\Omega_j\dot{q}_j(t) + \Omega_j^2 q_j(t) = \frac{1}{M_j}K_p V(t)\left[\phi_j'(x_1) - \phi_j'(x_0)\right], \tag{17}$$

where ζ_j is the j-th order damping coefficient.

Some corresponding physical parameters of the smart cantilever beam are given in Table 1. However, the smart structure has a nonlinear property, namely, the hysteresis phenomenon. Therefore, when the first order of the vibration modes of the beam with a piezoelectric actuator is considered with the Bouc–Wen equation, a dynamic model with hysteresis of the smart beam is derived from equation (16) as

$$\begin{cases} \ddot{q}_1(t) + 2\zeta_1\Omega\dot{q}_1(t) + \Omega_1^2 q_1(t) + A_z z(t) \\ \quad = \dfrac{1}{M_1}\left\{K_p V(t)\left[\phi_1'(x_1) - \phi_1'(x_0)\right]\right\}, \\ \dot{z}(t) = \alpha\dot{q}_1(t) - \beta\dot{q}_1(t)|z(t)|^n - \gamma|\dot{q}_1(t)||z(t)|^{n-1}z(t), \end{cases} \tag{18}$$

where $z(t)$ denotes the hysteresis item and the parameters A_z, n, α, β, and γ are used to obtain the form of the hysteresis property.

2.2. Model Identification by a Genetic Algorithm. For the above hysteresis parameters, A_z, α, β, and γ, a genetic identification algorithm [28, 29] is adopted to identify the hysteresis phenomenon of the smart beam. The parameters A_z, α, β, and γ are estimated by the input voltage and output response (bending deflection $\omega(x_0, t)$ at $x_0 = 0.115$ m) of the smart beam in the experiment. These estimated parameters are substituted in the original model to identify the output response. Therefore, an objective function is first defined as

$$f_s = \sqrt{\frac{\sum_{k=1}^{N}(X_k - \overline{X})^2}{N-1}}, \tag{19}$$

where f_s is the standard deviation, X_k is the k-th error between the identified data and experimental response, k is the sampling point, $\overline{X}$ is the average error, and N is the number of identified data points.

Before the genetic algorithm is implemented, some initial conditions are set. The maximum number of

Table 1: Corresponding parameters.

Beam	Piezoelectric	Others
$l_b = 0.4770\,\text{m}$	$l_p = 0.0280\,\text{m}$	$x_{11} = 2.4\,\text{cm}$
$h_b = 0.0305\,\text{m}$	$h_p = 0.0140\,\text{m}$	$x_{12} = 5.2\,\text{cm}$
$t_b = 0.7 \times 10^{-3}\,\text{m}$	$t_p = 0.3 \times 10^{-3}\,\text{m}$	$\zeta_1 = 0.042$
$E_b = 71\,\text{GPa}$	$E_p = 15.857\,\text{GPa}$	
$\rho_b = 2.77 \times 10^3\,\text{kg/m}^3$	$\rho_p = 5.44 \times 10^3\,\text{kg/m}^3$	
	$d_{31} = -1.7 \times 10^{-10}\,\text{C/N}$	

generations is MAXGEN = 100, the number of individuals is NIND = 100, the crossover probability and mutation probability are 0.7 and 0.02, respectively, and the generation gap is GGAP = 0.8. The default ranges of the identified parameters in Table 2 are very important for the convergence rate of the iterations for the genetic algorithm. Moreover, the experimental response is collected with a laser displacement sensor when a sinusoidal voltage $V = 150 \times \sin(2\pi \times 2.5t)$ is applied to the piezoelectric actuator. Therefore, with the input voltage and output response data from the experiment, the identified parameters A_z, α, β, and γ are obtained in the default ranges, as shown in Table 2.

Figure 2 shows the convergence of the genetic algorithm when the hysteresis parameters A_z, α, β, and γ are identified. The minimum standard deviation converges to a stable state after a generation number of approximately 20. Moreover, when the identified parameters in the third column of Table 2 at the last generation number 100 are substituted into equation (18), the identified displacement is obtained and compared with the experimental displacement in Figure 3(a), and a part of Figure 3(a) from 26 s to 28 s is magnified in Figure 3(b). Then, to display the detailed hysteresis property, a period of experimental and identified data is excerpted from Figure 3(a) and is shown Figure 4. The red identified discrete data are consistent with the blue experimental solid curve. As a result, the dynamic model equation (18) is valid for describing the hysteresis property of the smart cantilever beam with the genetic identification algorithm.

2.3. Stability Analysis for the Bouc–Wen Model. For the constructed dynamic model, the stability of the identified system is analyzed. Based on the above identified parameters, equation (18) is first transferred as

$$\begin{bmatrix} \dot{u}_1 \\ \dot{u}_2 \\ \dot{u}_3 \end{bmatrix} = \begin{bmatrix} u_3 \\ \alpha \dot{q}_1(t) - \beta \dot{q}_1(t)|z(t)|^n - \gamma |\dot{q}_1(t)||z(t)|^{n-1} z(t) \\ -2\zeta_1 \Omega \dot{q}_1(t) - \Omega_1^2 q_1(t) - A_z z(t) \end{bmatrix} + \begin{bmatrix} 0 \\ 0 \\ \dfrac{K_p[\phi_1'(x_1) - \phi_1'(x_0)]}{M_1} \end{bmatrix} V(t), \tag{20}$$

where $u_1 = q_1$, $u_2 = z$, and $u_3 = \dot{q}_1$.

Table 2: The identified parameters.

Parameters	Default ranges	Identified values
A_z	[0, 0.5]	0.110
α	[0, 0.5]	0.4971
β	[0, 0.5]	0.2636
γ	[0.5, 1]	0.8282

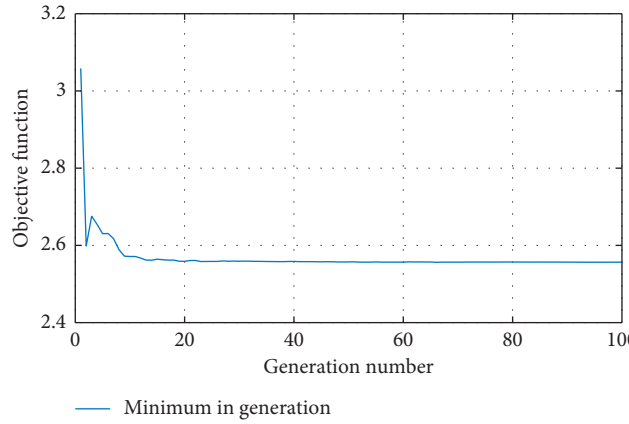

Figure 2: Convergence of the genetic algorithm.

Then, if $n = 1$, a further equation simplification is made and equation (20) is expressed as

$$\begin{bmatrix} \dot{u}_1 \\ \dot{u}_2 \\ \dot{u}_3 \end{bmatrix} = \begin{bmatrix} u_3 \\ \alpha u_3 - (\delta_1 \beta + \delta_2 \gamma) u_3 u_2 \\ -2\zeta_1 \Omega u_3 - \Omega_1^2 u_1 - A_z u_2 \end{bmatrix} + \begin{bmatrix} 0 \\ 0 \\ D_V \end{bmatrix} V(t), \tag{21}$$

where $\delta_1 = 1$ when $u_2 > 0$, $\delta_1 = -1$ and $\delta_2 = 1$ when $u_3 > 0$, and $\delta_2 = -1$. $D_V = (K_p[\phi_1'(x_1) - \phi_1'(x_0)]/M_1)$.

Next, equation (21) is given in vector form as

$$\dot{\mathbf{u}} = \mathbf{P}(\mathbf{u}) + \mathbf{D}_V V(t), \tag{22}$$

where

$$\mathbf{u} = [u_1 \;\; u_2 \;\; u_3]^T, \quad \mathbf{P}(\mathbf{u}) = \begin{bmatrix} u_3 \\ \alpha u_3 - (\delta_1 \beta + \delta_2 \gamma) u_3 u_2 \\ -2\zeta_1 \Omega u_3 - \Omega_1^2 u_1 - A_z u_2 \end{bmatrix}, \quad \mathbf{D}_V = [0 \;\; 0 \;\; D_V]^T. \tag{23}$$

If $\mathbf{P}(\mathbf{u}_s) = 0$, $\mathbf{u}_s$ is the equilibrium point in the phase plane. By the nonlinear function $\mathbf{P}(\mathbf{u})$, $\mathbf{u}_s = [u_{s1} \;\; u_{s2} \;\; 0]^T$ and $u_{s2} = -(\Omega_1^2/A_z)u_{s1}$. Therefore, the stability analyses of equation (22) are explored near the equilibrium point $\mathbf{u}_s$. In addition, equation (22) without external excitation voltage is written as

$$\dot{\mathbf{u}} = D\mathbf{P}(\mathbf{u}_s) * (\mathbf{u} - \mathbf{u}_s) + O\left(\|\mathbf{u} - \mathbf{u}_s\|^2\right), \tag{24}$$

where

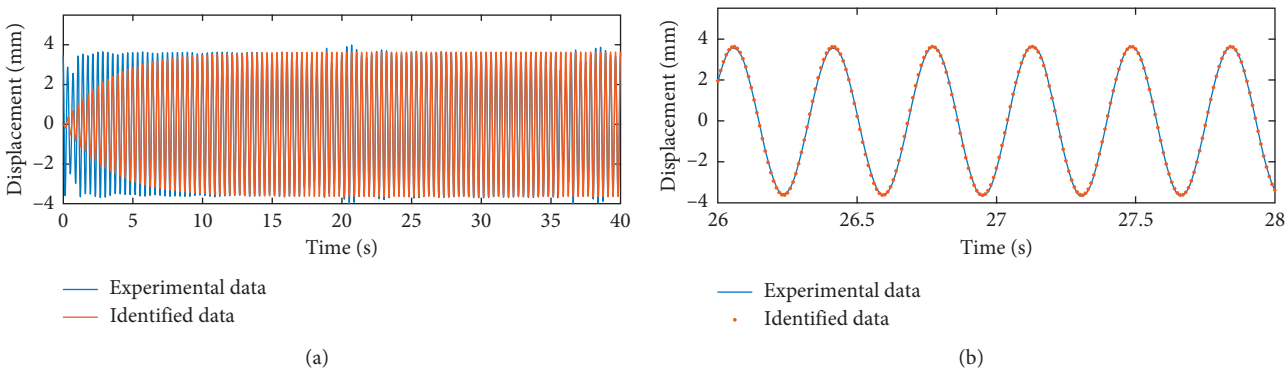

FIGURE 3: Comparison of the experimental displacement with the identified result. (a) Identified and experimental displacement responses. (b) Magnification of a part of Figure 3(a) from 26 s to 28 s.

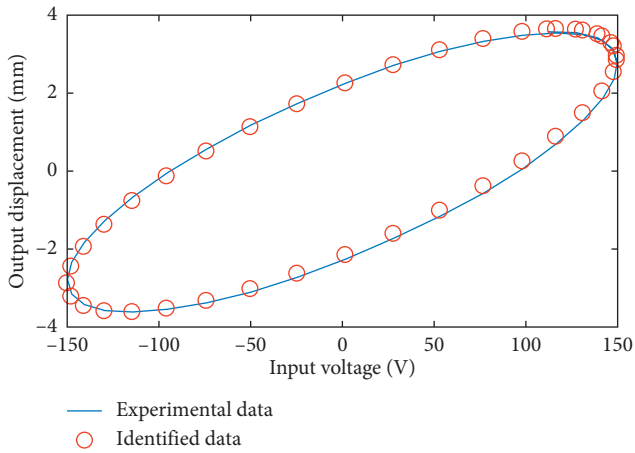

FIGURE 4: Hysteresis loop of the experiment and identification.

$$D\mathbf{P}(u) = \begin{bmatrix} 0 & 0 & 1 \\ 0 & -(\delta_1\beta + \delta_2\gamma)u_3 & \alpha - (\delta_1\beta + \delta_2\gamma)u_{s2} \\ -\Omega_1^2 & -A_z & -2\zeta_1\Omega \end{bmatrix} \begin{bmatrix} du_1 \\ du_2 \\ du_3 \end{bmatrix}, \tag{25}$$

and $O(\cdot)$ is the minimum value of approximately $\|\mathbf{u} - \mathbf{u}_s\|^2$.

Therefore, equation (23) is simplified as

$$\dot{\mathbf{u}} = \mathbf{A}_\lambda(\mathbf{u} - \mathbf{u}_s), \tag{26}$$

where

$$\mathbf{A}_\lambda = \begin{bmatrix} 0 & 0 & 1 \\ 0 & -(\delta_1\beta + \delta_2\gamma)u_3 & \alpha - (\delta_1\beta + \delta_2\gamma)u_2 \\ -\Omega_1^2 & -A_z & -2\zeta_1\Omega \end{bmatrix}\Bigg|_{u=u_s} = \begin{bmatrix} 0 & 0 & 1 \\ 0 & 0 & \alpha - (\delta_1\beta + \delta_2\gamma)u_{s2} \\ -\Omega_1^2 & -A_z & -2\zeta_1\Omega \end{bmatrix}. \tag{27}$$

Furthermore, the eigenvalues λ are calculated by the following equation:

$$|\lambda\mathbf{I} - \mathbf{A}_\lambda| = 0, \tag{28}$$

where $\mathbf{I}$ is the unit matrix.

By equation (28), the characteristic equation is derived as

$$\lambda\left\{\lambda^2 + 2\xi\Omega_1\lambda + A_z[\alpha - (\delta_1\beta + \delta_2\gamma)u_{s2}] + \Omega_1^2\right\} = 0. \tag{29}$$

If the system is stabilized, the real parts of its eigenvalues are negative. As a result, the third item plus the fourth item is greater than zero and is given as

$$0 < A_z[\alpha - (\delta_1\beta + \delta_2\gamma)u_{s2}] + \Omega_1^2. \tag{30}$$

Finally, for the stabilized model of smart beam, the relation between the identified parameters A_z, α, β, and γ is presented as

$$A_z(\delta_1\beta + \delta_2\gamma)u_{s2} < (\alpha A_z + \Omega_1^2). \tag{31}$$

If $u_{s2} = 0$, then

$$-\Omega_1^2 < \alpha A_z. \tag{32}$$

According to the identified parameter values in Table 2, assuming $A_z = 0.110a_z$, the smart beam system is stable at $a_z > -4.5044$ from equation (32).

3. Model Reference Adaptive Control with the Bouc–Wen Model

3.1. Adaptive Control Law. In this paper, the vibration suppression problem of a smart beam considering the hysteresis property is explored by using a model reference adaptive control (MRAC) [22, 25]. For adaptive control, a reference model is assumed as an expected objective model. According to the error between the output states of the smart beam and the expected objective hysteresis model, the adaptive control law is designed online with gains K_r and K_u, as shown in Figure 5.

First, the expected objective hysteresis model is given as

$$\ddot{u}_{eo} = -2\zeta_{eo}\Omega_1\dot{u}_{eo} - \Omega_1^2 u_{eo} - a_z A_z z + D_V u_r, \tag{33}$$

where ζ_{eo} is set as 0.707, a_z is a hysteresis coefficient, and $a_z A_z$ satisfies equation (32).

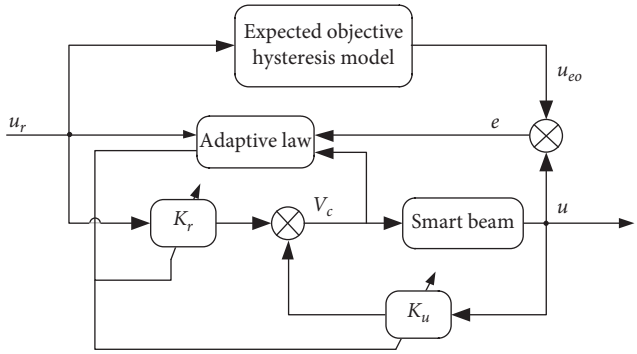

Figure 5: Model reference adaptive control.

$$V_c = K_r u_r + K_u u. \tag{34}$$

Substituting equation (34) into equation (18), the identified model is derived as

$$\ddot{u} = -2\zeta_1\Omega_1\dot{u} - \Omega_1^2 u - A_z z + D_V K_r u_r + D_V K_u u. \tag{35}$$

Then, the error between the outputs of the expected objective model and the smart beam is expressed as

$$e = u_{eo} - u. \tag{36}$$

Furthermore, equation (36) is transformed into a state-space equation with equations (33) and (37), which is displayed as

$$\begin{aligned}\begin{bmatrix}\dot{e}\\ \ddot{e}\end{bmatrix} &= A_{eo}\begin{bmatrix}e\\ \dot{e}\end{bmatrix} + \left(A_{eo} - A_u - B_u K_u\right)\begin{bmatrix}u\\ \dot{u}\end{bmatrix}\\ &\quad - \left(B_{eo} - B_u K_r\right)u_r + \begin{bmatrix}0\\ a_z - 1\end{bmatrix}A_z z,\end{aligned} \tag{37}$$

where

$$\begin{aligned}A_{eo} &= \begin{bmatrix}0 & 1\\ -\Omega_1^2 & -2\xi_{eo}\Omega_1\end{bmatrix},\\ A_u &= \begin{bmatrix}0 & 1\\ -\Omega_1^2 & -2\xi_1\Omega_1\end{bmatrix},\\ B_{eo} &= \begin{bmatrix}0\\ D_{Veo}\end{bmatrix},\\ B_u &= \begin{bmatrix}0\\ D_V\end{bmatrix}.\end{aligned} \tag{38}$$

If the second item and the third item on the right of equation (37) are equal to zero, the error e of equation (36) is convergent and $\lim_{t\longrightarrow\infty} e(t) = 0$. The fourth item of equation (36) is only considered when the influence of hysteresis on the control effect is studied. Therefore, the control gains $K_r(t \longrightarrow \infty) = K_{r\infty}$ and $K_u(t \longrightarrow \infty) = K_{u\infty}$ must satisfy the following equations:

$$\begin{cases}A_{eo} - A_u - B_u K_{u\infty} = 0,\\ B_{eo} - B_u K_{r\infty} = 0,\end{cases} \tag{39}$$

or

$$\begin{cases}A_u = A_{eo} - B_u K_{u\infty}^{-1},\\ B_u = B_{eo} K_{r\infty}^{-1}.\end{cases} \tag{40}$$

Moreover, substituting equation (40) into equation (37) yields

$$\dot{e} = A_{eo}\mathbf{e} + B_{eo}K_r^{-1}\overline{K}_u\mathbf{u} + B_{eo}K_r^{-1}\overline{K}_r u_r + (a_z - 1)A_z z, \tag{41}$$

where $\mathbf{e} = \begin{bmatrix}e & \dot{e}\end{bmatrix}^T$, $\overline{K}_u = K_{u\infty} - K_u$, and $\overline{K}_r = K_{r\infty} - K_r$.

Furthermore, for the stability analyses of the control system, a Lyapunov function is constructed as

$$V = \mathbf{e}^T\mathbf{P}\mathbf{e} + \mathrm{trace}\left(\overline{K}_u^T\mathbf{P}_u^{-1}\overline{K}_u\right) + \mathrm{trace}\left(\overline{K}_r^T\mathbf{P}_r^{-1}\overline{K}_r\right), \tag{42}$$

where $\mathbf{P}$, $\mathbf{P}_u$, and $\mathbf{P}_r$ are positive definite matrices. In addition, trace $(\cdot)$ calculates the trace of a matrix.

For equation (42), the derivative is obtained as

$$\begin{aligned}\dot{V} &= \dot{e}^T\mathbf{P}\mathbf{e} + \mathbf{e}^T\mathbf{P}\dot{e} + \mathrm{trace}\left(\dot{\overline{K}}_u^T\mathbf{P}_u^{-1}\overline{K}_u + \overline{K}_u^T\mathbf{P}_u^{-1}\dot{\overline{K}}_u\right)\\ &\quad + \mathrm{trace}\left(\dot{\overline{K}}_r^T\mathbf{P}_r^{-1}\overline{K}_r + \overline{K}_r^T\mathbf{P}_r^{-1}\dot{\overline{K}}_r\right).\end{aligned} \tag{43}$$

Substituting equation (41) into equation (43) yields

$$\begin{aligned}\dot{V} &= \mathbf{e}^T\left(A_{eo}^T\mathbf{P} + \mathbf{P}A_{eo}\right)\mathbf{e} + 2\mathrm{trace}\left(\dot{\overline{K}}_u^T\mathbf{P}_u^{-1}\overline{K}_u + \mathbf{u}\mathbf{e}^T\mathbf{P}B_{eo}K_{u\infty}^{-1}\overline{K}_u\right)\\ &\quad + 2\mathrm{trace}\left(\dot{\overline{K}}_r^T\mathbf{P}_r^{-1}\overline{K}_r + \mathbf{u}_r\mathbf{e}^T\mathbf{P}B_{eo}K_{r\infty}^{-1}\overline{K}_r\right).\end{aligned} \tag{44}$$

If the first item of equation (44) is negative, namely, $A_{eo}^T\mathbf{P} + \mathbf{P}A_{eo} = -\mathbf{Q}$, $\mathbf{Q}$ is a positive definite matrix. Therefore, the second and third items are equal to zero. With $\overline{K}_u = K_{u\infty} - K_u$ and $\overline{K}_r = K_{r\infty} - K_r$, the control gain matrices K_u and K_r are expressed as

$$\begin{cases}\dot{K}_u = R_1 B_{eo}\mathbf{P}\mathbf{e}\mathbf{u}^T,\\ \dot{K}_r = R_2 B_{eo}\mathbf{P}\mathbf{e}\mathbf{u}_r^T,\end{cases} \tag{45}$$

where $R_1 = \mathbf{P}_u(K_{u\infty}^{-1})^T$ and $R_2 = \mathbf{P}_r(K_{u\infty}^{-1})^T$.

If the actual control gains are realized in discrete form, equation (45) is also represented as

$$\begin{cases}K_u(k) = K_u(k-1) + h \times R_1 B_{eo}\mathbf{P}\mathbf{e}\mathbf{u}^T,\\ K_r(k) = K_r(k-1) + h \times R_2 B_{eo}\mathbf{P}\mathbf{e}\mathbf{u}_r^T,\end{cases} \tag{46}$$

where k is the sampling point and h is the sampling interval.

4. Simulation and Experimental Verifications of Model Reference Adaptive Control

4.1. Simulation Verifications. After a hysteresis model is constructed and an adaptive control law is designed, a numerical simulation is implemented in MATLAB/Simulink. The adaptive control law with the hysteresis model in MATLAB/Simulink is solved with the Runge–Kutta method (ODE45). How the hysteresis property affects the adaptive control effect for the smart beam is explored with numerical simulation analyses.

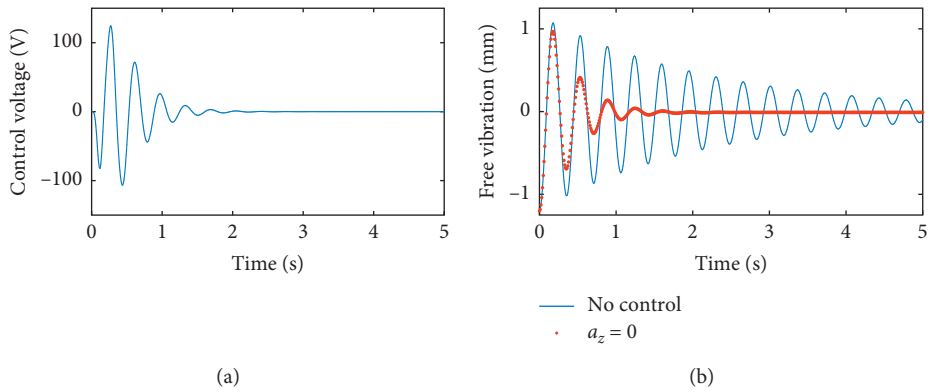

Figure 6: Control result at $a_z = 0$. (a) Control voltage (b) Free vibration.

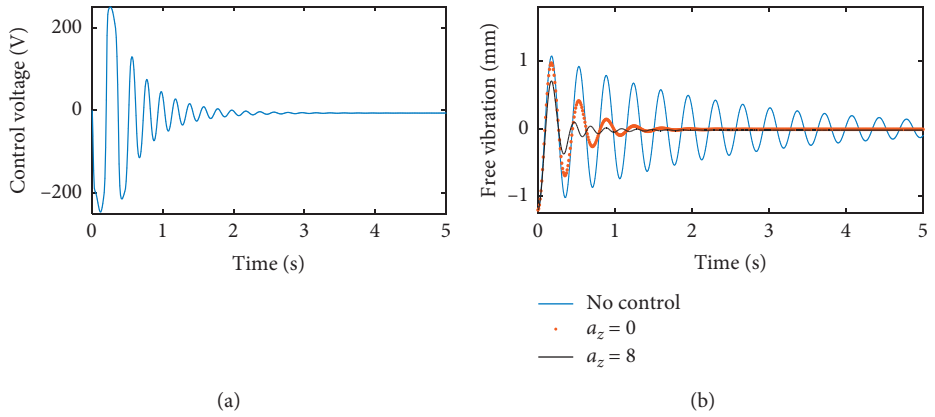

Figure 7: Control result at $a_z = 8$. (a) Control voltage (b) Free vibration.

Figure 6 shows the control result with no hysteresis in the expected objective hysteresis model of equation (33). Figure 6(a) shows the control voltage. Moreover, Figure 6(b) displays the free vibration of the cantilever beam with adaptive control at $a_z = 0$ compared with the result with no control. If the hysteresis coefficient a_z changes, the control result for the free vibration of the smart beam is different. When the hysteresis coefficient a_z is set to $-4, -3, \ldots, 8, \ldots$, it is found that the control effect at $a_z = 8$ is the best.

Figure 7 shows the control result considering the hysteresis property in the expected objective hysteresis model at $a_z = 8$. Figure 7(a) shows the control voltage and Figure 7(b) presents the free vibration of the smart beam at $a_z = 8$ compared with that at $a_z = 0$. Obviously, the vibration amplitude at $a_z = 8$ is less than that at $a_z = 0$. Figure 8 displays the frequency response of the curves in Figure 7(b) obtained by a fast Fourier transform (FFT). The amplitude peak value of the frequency response at $a_z = 8$ is 0.03083 mm, the amplitude peak value of the frequency response at $a_z = 0$ is 0.05875 mm, and the amplitude peak value of the frequency response with no control is 0.2567 mm. The control effect considering the hysteresis property in the expected objective hysteresis model at $a_z = 8$ is superior to that with a linear expected objective model at $a_z = 0$.

When the hysteresis coefficient a_z changes from −4 to 15, the amplitude peak values of the frequency response are given in Figure 9(a). If the practical time delay of the sensor and the processing time spent in the computer are not considered in the simulation, the amplitude peak value of the frequency response tends to be constant under a limited control voltage applied by the power equipment with hysteresis item a_z gradually increasing. Moreover, when the hysteresis coefficient a_z is less than −4, the control system of the smart beam is not stable. However, when the time delay

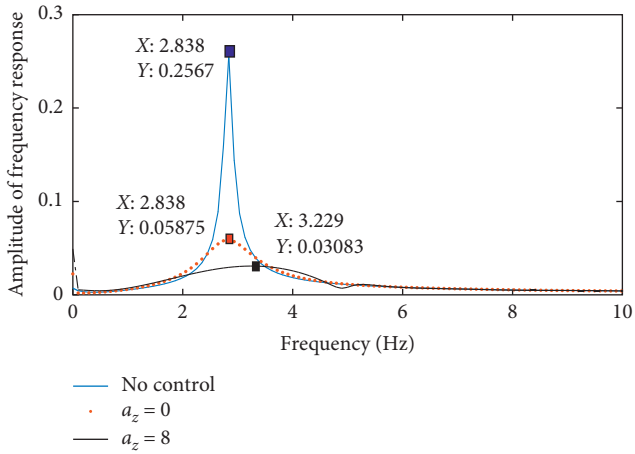

Figure 8: Amplitude-frequency characteristic of the free vibration.

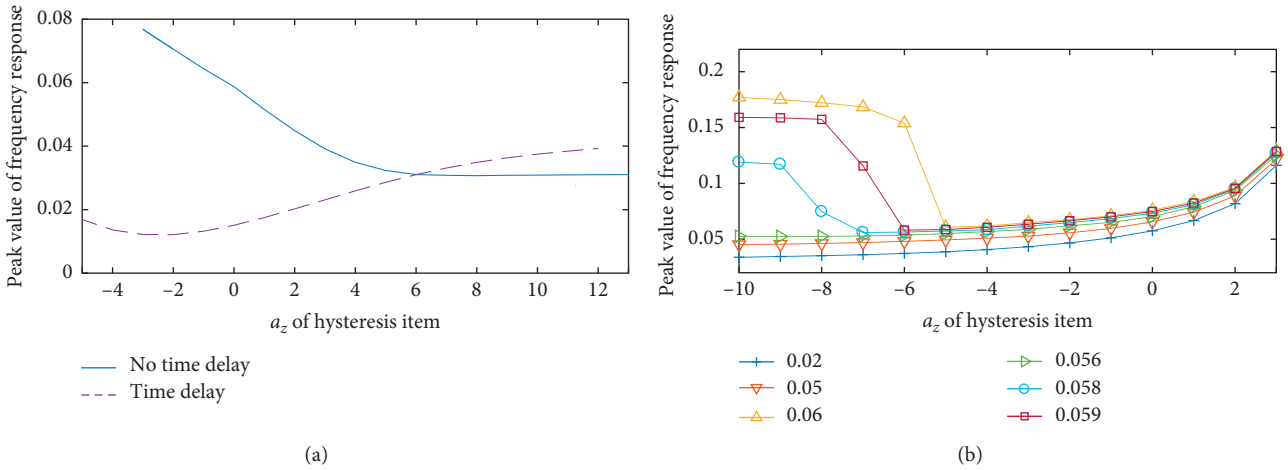

Figure 9: Peak of the amplitude-frequency characteristic curve. (a) Curves with and without time delay. (b) Curves with different time delays.

of the sensing data and the processing time of the PC are added in the closed-loop control in the simulation, the control system of the smart beam is not stable at $a_z < 5$ and $a_z > 12$. The amplitude peak value of the frequency response at approximately $a_z = -2$ is the minimum of the dotted curve in Figure 9(a). Figure 9(b) shows peak of amplitude-frequency characteristic curves with different time delays (0.02 s, 0.05 s, 0.056 s, 0.058 s, 0.059 s, and 0.06 s), and the limited peak value is the minimum at $a_z = -5$, -6, and -7, when the time delay are set to 0.06 s, 0.059 s, and 0.058 s, respectively. Moreover, different time delays will affect the stability of the control system. Therefore, adding the time delay in the closed-loop control system will produce a different control result.

4.2. Experimental Verifications. An experimental platform is set up to verify the vibration control effect of the smart beam by the adaptive model reference control with a Bouc–Wen model as the expected objective model. The experimental equipment is shown in Figure 10. The adaptive control law is realized in LabVIEW. The control voltage is transported to the data acquisition unit. A power supply is used to amplify the control voltage from the data acquisition unit. Then, the control voltage is applied to the piezoelectric patch to suppress the vibration of the cantilever beam when the beam suffers from an initial disturbance. A laser displacement sensor is used to sense the bending deflection of the smart beam.

Figure 11 shows the vibration control result at $a_z = 0$ for the smart beam. Figure 11(a) shows the control voltage, while Figure 11(b) displays the free vibration of the beam when the initial displacement at the free end of the beam is approximately 2 cm. It is observed easily that the vibration amplitude with control at $a_z = 0$ is 0.15 mm at 0.45 s. Furthermore, Figure 12 shows the control result at $a_z = -6$. Figure 12(a) shows the control voltage, and Figure 12(b) displays the free vibration of the cantilever beam with control at $a_z = -6$. Compared with the vibration amplitude at $a_z = 0$, the vibration amplitude $a_z = -6$ is 0.09 mm at

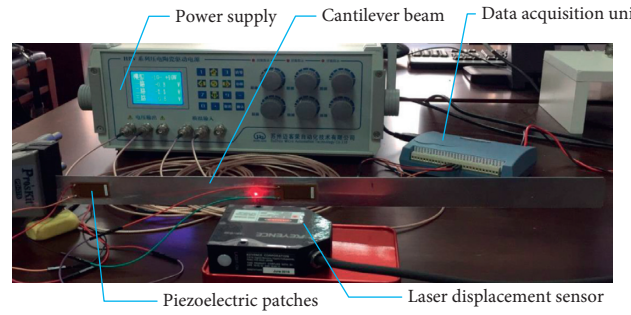

Figure 10: Experimental equipment.

0.4 s. Notably, the control effect at $a_z = -6$ is better than that at $a_z = 0$.

Similarly, the frequency response of the three curves in Figure 12(b) is shown in Figure 13. The amplitude peak of the frequency response at $a_z = -6$ is 0.01157 mm at a frequency of 5.2490 Hz, the amplitude peak of the frequency response at $a_z = 0$ is 0.02431 mm at a frequency of 8.8060 Hz, and the amplitude peak of the frequency response with no control is 0.2063 mm at a frequency of 2.5740 Hz. It is clearly indicated that the vibration control effect $a_z = -6$ for the cantilever beam is better than that at $a_z = 0$.

When the hysteresis coefficient a_z changes, the peak value in the experiment exhibits the same changing trend in contrast to the result of the simulation considering the time delay in closed-loop control system, as shown in Figure 14. The solid curve is a polyfit of the curve from the experiment. The dashed curve is the amplitude peak value of the frequency response from the simulation considering the time delay. Then, both the solid curve and the dashed curve have their own minimum peak values. However, the hysteresis coefficients a_z of the two minimum peak values are different. One value is -2 and the other value is -6. The deviation between the experiment and simulation is caused by the time delay. In the experimental system, the time delay includes not only the sensing delay of the sensor but also the processing time of the PC. The sensing delay of the sensor is

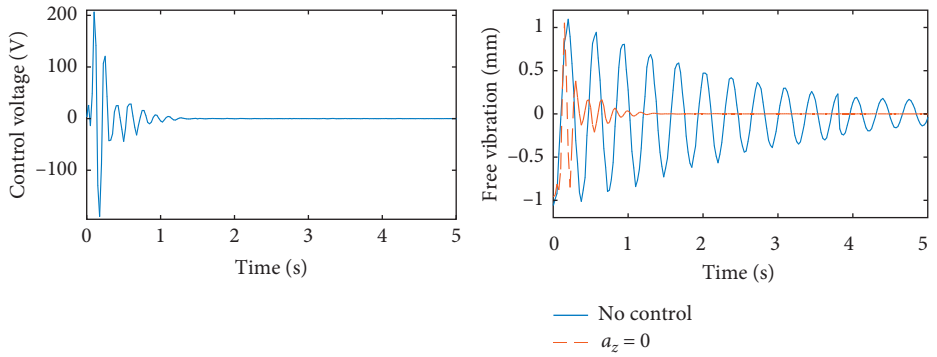

Figure 11: Control result at $a_z = 0$.

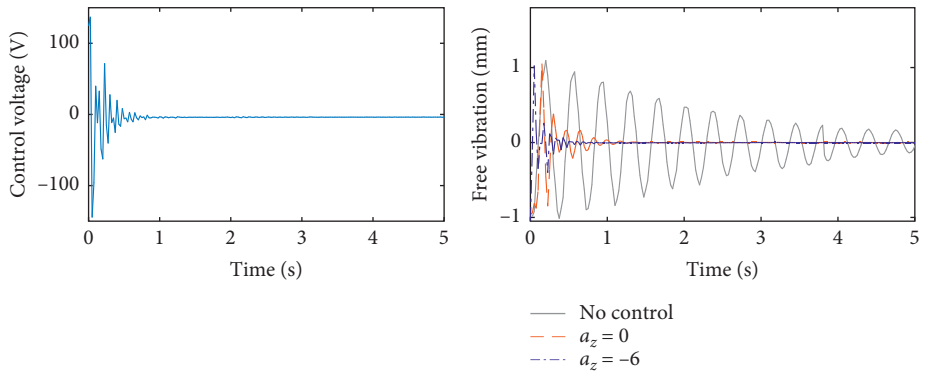

Figure 12: Control result at $a_z = -6$.

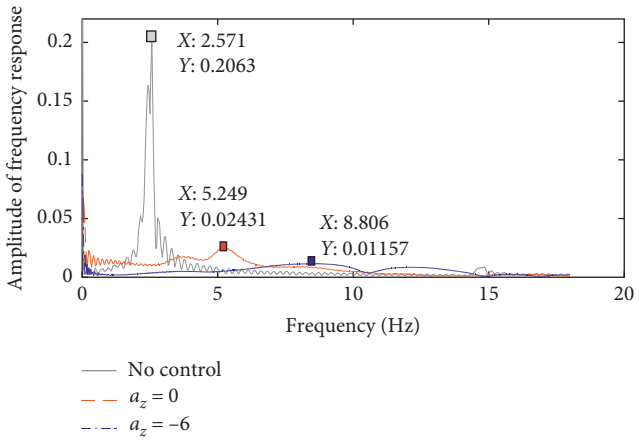

Figure 13: Amplitude-frequency characteristic of the free vibration.

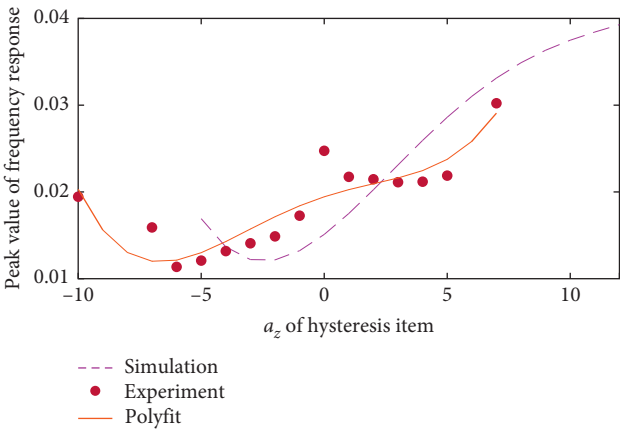

Figure 14: Peak of the amplitude-frequency characteristic curve.

obtained from the user manual of the sensor. However, the processing time of the PC in the simulation is not calculated accurately. When too many application programs are running on the computer, the processing velocity of the PC slows down and the processing time of PC is large, and vice versa.

Through the simulation and experimental verifications, adaptive model reference control with a Bouc–Wen model as an expected objective model is proven to be feasible for suppressing the vibration of the cantilever beam when it suffers from an initial displacement at the free end. It is illustrated that the hysteresis property will affect the stability and control effect of the control system when considering the time delay.

5. Conclusion

In this paper, a Bouc–Wen model is constructed with a genetic identification algorithm to describe the hysteresis property of a smart beam with a piezoelectric actuator. With the identification result, the identified hysteresis loop can be

consistent with the experimental hysteresis loop. Based on the hysteresis model as an expected objective model, a stability analysis of the smart system is presented, and adaptive model reference control is designed to explore the influence of the hysteresis characteristic on the control effect. By the simulation and experimental verifications, adaptive model reference control is demonstrated to be feasible for suppressing the vibration of the cantilever beam and the hysteresis item in the expected objective model will affect the stability and control effect of adaptive control for the smart beam with a time delay.

Nomenclature

Bouc–Wen model:	A hysteresis model
PID:	Proportional, integral, and differential control
LQR:	Linear quadratic regulator
Preisach model:	A hysteresis model
PI model:	A hysteresis model
MAXGEN:	The maximum number of generations
NIND:	The number of individuals
GGAP:	The generation gap
MRAC:	Model reference adaptive control
ODE45:	A numerical solution method for an ordinary differential equation
FFT:	Fast Fourier transform
PC:	Personal computer.

Data Availability

The data used to support the findings of this study are available from the corresponding author upon request.

Conflicts of Interest

The authors declare that there are no conflicts of interest regarding the publication of this paper.

Acknowledgments

This work was supported by the National Natural Science Foundation of China (11702168 and 11602135).

References

[1] F. Wolf, A. Sutor, S. J. Rupitsch, and R. Lerch, "Modeling and measurement of creep- and rate- dependent hysteresis in ferroelectric actuators," *Sensors and Actuators A: Physical*, vol. 172, no. 1, pp. 245–252, 2011.

[2] M. S. Rana, H. R. Pota, and I. R. Petersen, "Nonlinearity effect reduction of an AFM piezoelectric tube scanner using MIMO MPC," *IEEE/ASME Transactions on Mechatronics*, vol. 20, no. 3, pp. 1458–1469, 2015.

[3] G.-Y. Gu and L.-M. Zhu, "Motion control of piezoceramic actuators with creep, hysteresis and vibration compensation," *Sensors and Actuators A: Physical*, vol. 197, pp. 76–87, 2013.

[4] S. R. Viswamurthy and R. Ganguli, "Effect of piezoelectric hysteresis on helicopter vibration control using trailing-edge flaps," *Journal of Guidance, Control, and Dynamics*, vol. 29, no. 5, pp. 1201–1209, 2006.

[5] R. Mallick, R. Ganguli, and M. S. Bhat, "An experimental and numerical study of piezoceramic actuator hysteresis in helicopter active vibration control," *Proceedings of the Institution of Mechanical Engineers, Part G: Journal of Aerospace Engineering*, vol. 228, no. 5, pp. 690–705, 2014.

[6] T. Sangpet, S. Kuntanapreeda, and R. Schmidt, "An adaptive PID-like controller for vibration suppression of piezo-actuated flexible beams," *Journal of Vibration and Control*, vol. 24, no. 12, pp. 2656–2670, 2018.

[7] Q. Xu and Y. Li, "Model predictive discrete-time sliding mode control of a nanopositioning piezostage without modeling hysteresis," *IEEE Transactions on Control Systems Technology*, vol. 20, no. 4, pp. 983–994, 2012.

[8] S. Zhang, R. Schmidt, and X. Qin, "Active vibration control of piezoelectric bonded smart structures using PID algorithm," *Chinese Journal of Aeronautics*, vol. 28, no. 1, pp. 305–313, 2015.

[9] O. Abdeljaber, O. Avci, and D. J. Inman, "Active vibration control of flexible cantilever plates using piezoelectric materials and artificial neural networks," *Journal of Sound and Vibration*, vol. 363, pp. 33–53, 2016.

[10] H. Habibullah, H. R. Pota, and I. R. Petersen, "A robust control approach for high-speed nanopositioning applications," *Sensors and Actuators A: Physical*, vol. 292, pp. 137–148, 2019.

[11] A. Badel, R. Le Breton, F. Formosa, S. Hanene, and J. Lottin, "Precise positioning and active vibration isolation using piezoelectric actuator with hysteresis compensation," *Journal of Intelligent Material Systems and Structures*, vol. 25, no. 2, pp. 155–163, 2014.

[12] S. H. Chung and E. H. K. Fung, "A nonlinear finite element model of a piezoelectric tube actuator with hysteresis and creep," *Smart Materials and Structures*, vol. 19, no. 4, Article ID 045028, 2010.

[13] M. Al Janaideh, M. Rakotondrabe, and O. Aljanaideh, "Further results on hysteresis compensation of smart micropositioning systems with the inverse Prandtl-ishlinskii compensator," *IEEE Transactions on Control Systems Technology*, vol. 24, no. 2, pp. 428–439, 2016.

[14] M. Al Janaideh and P. Krejci, "Inverse rate-dependent Prandtl-ishlinskii model for feedforward compensation of hysteresis in a piezomicropositioning actuator," *IEEE/ASME Transactions on Mechatronics*, vol. 18, no. 2, pp. 1498–1507, 2013.

[15] D. H. Wang and W. Zhu, "A phenomenological model for pre-stressed piezoelectric ceramic stack actuators," *Smart Materials and Structures*, vol. 20, no. 3, Article ID 035018, 2011.

[16] J. Q. Gan and X. M. Zhang, "A review of nonlinear hysteresis modeling and control of piezoelectric actuators," *AIP Advances*, vol. 9, no. 4, Article ID 040702, 2019.

[17] W. Guo, D. Liu, and W. Wang, "Neural network hysteresis modeling with an improved Preisach model for piezoelectric actuators," *Engineering Computations*, vol. 29, no. 3, pp. 248–259, 2012.

[18] Y. Wu and M. Deng, "Experimental study on robust nonlinear forced vibration control for an L-shaped arm with reduced control inputs," *IEEE/ASME Transactions on Mechatronics*, vol. 22, no. 5, pp. 2186–2195, 2017.

[19] D. Habineza, M. Rakotondrabe, and Y. L. Gorrec, "Multivariable generalized Bouc-Wen modeling, identification and feedforward control and its application to multi-DoF piezoelectric actuators," *IFAC Proceedings Volumes*, vol. 47, no. 3, pp. 10952–10958, 2014.

[20] M. S. Sofla, F. Barazandeh, S. M. Rezaei, M. Zareinejad, and M. Saadat, "Observer-based robust motion control of a piezo-actuated stage under external disturbances," *Transactions of the Institute of Measurement and Control*, vol. 34, no. 4, pp. 365–375, 2012.

[21] Y. Zhang, Z. Chen, Y. Jiao, and X. Wang, "Hysteresis linearization control of a novel hybrid vibration isolator," *Journal of Vibroengineering*, vol. 19, no. 3, pp. 1557–1568, 2017.

[22] M. H. Salah, M. L. McIntyre, D. M. Dawson, J. R. Wagner, and E. Tatlicioglu, "Charge feedback-based robust position tracking control for piezoelectric actuators," *IET Control Theory & Applications*, vol. 6, no. 5, pp. 615–628, 2012.

[23] H. Yang, W. Zhu, and X. Fu, "Robust model reference adaptive control for a two-dimensional piezo-driven micro-displacement scanning platform based on the asymmetrical Bouc-Wen model," *AIP Advances*, vol. 6, no. 11, Article ID 115308, 2016.

[24] N. Chuang, I. R. Petersen, and H. R. Pota, "Robust H∞, control in fast atomic force microscopy," *Asian Journal of Control*, vol. 15, no. 3, pp. 872–887, 2013.

[25] R. Svečko and D. Kusić, "Feedforward neural network position control of a piezoelectric actuator based on a BAT search algorithm," *Expert Systems with Applications*, vol. 42, no. 13, pp. 5416–5423, 2015.

[26] W. Li and X. Chen, "Compensation of hysteresis in piezoelectric actuators without dynamics modeling," *Sensors and Actuators A: Physical*, vol. 199, pp. 89–97, 2013.

[27] S. K. Das, H. R. Pota, and I. R. Petersen, "A MIMO double resonant controller design for nanopositioners," *IEEE Transactions on Nanotechnology*, vol. 14, no. 2, pp. 224–237, 2015.

[28] W. Zhu and D.-H. Wang, "Non-symmetrical Bouc–Wen model for piezoelectric ceramic actuators," *Sensors and Actuators A: Physical*, vol. 181, pp. 51–60, 2012.

[29] V. Hassani, T. Tjahjowidodo, and T. N. Do, "A survey on hysteresis modeling, identification and control," *Mechanical Systems and Signal Processing*, vol. 49, no. 1-2, pp. 209–233, 2014.